Faraday Discussions

Cite this: *Faraday Discuss.*, 2026, **264**, 474

ROYAL SOCIETY OF CHEMISTRY

PAPER

View Article Online
View Journal | View Issue

Optical responses from high-entropy alloys: experimental results and perspectives

Alexandre Nominé, *[ab] Alexander I. Solomonov, [c] Juš Polanšek,[b] Maxime Vergès,[a] Yann Battie, [d] Stéphanie Bruyère,[a] Jaafar Ghanbaja,[a] Jean-François Pierson, [a] Janez Zavašnik, [be] Michael Feuerbacher,[f] Uroš Cvelbar, [b] Thierry Belmonte[a] and Valentin Milichko*[ag]

Received 19th May 2025, Accepted 21st August 2025
DOI: 10.1039/d5fd00086f

High-entropy alloys (HEAs) combine five or more elements in near-equiatomic ratios, opening an immense compositional space whose optical behaviour is still largely unknown. Phase-modulated ellipsometry on bulk CrMnFeCoNi (Cantor) shows that its intrinsic optical constants, n, k, ε_1 and ε_2, deviate strongly from the arithmetic means of the constituent elements—by up to a factor of two beyond 1 μm—yet the derived functional responses, reflectance R and absorption coefficient α, are reproduced to within ∼20%. Cantor nanoparticles have been produced by nanosecond electric discharges in liquid nitrogen. Dark-field spectroscopy and Mie calculations reveal a dominant scattering mode near 100 nm that red-shifts and broadens with increasing size; the steady-state photothermal rise calculated from the absorption cross-section σ_{abs} falls between those of the constituent pure metals. Generalising the averaging rule, we compute proxy values of R and α for 10 994 density-functional-theory-predicted HEAs. Successive optical, thermal and resource filters condense the space to 58 candidates at 355 nm and eight refractory alloys at 1064 nm, illustrating a "sustainable-by-design" route for future HEA photonics.

[a]*Institut Jean Lamour – Univ. Lorraine/CNRS, Nancy, France. E-mail: alexandre.nomine@univ-lorraine.fr; valentin.milichko@univ-lorraine.fr*
[b]*Jožef Stefan Institute, Jamova Cesta 39, SI-1000 Ljubljana, Slovenia*
[c]*School of Physics and Engineering, ITMO University, St. Petersburg, Russia*
[d]*Laboratoire de Chimie et Physique, Approche Multi-Echelle des Milieux Complexes, Univ. Lorraine, Metz, France*
[e]*Max-Planck Institute for Sustainable Materials, Max-Planck-Straße 1, 40237 Düsseldorf, Germany*
[f]*Ernst Ruska-Centre for Microscopy and Spectroscopy with Electrons, Forschungszentrum Jülich, 52425 Jülich, Germany*
[g]*School of Engineering, New Uzbekistan University, Tashkent, 100007, Uzbekistan*

Introduction

High-entropy alloys (HEAs) emerged as a revolutionary class of materials in the early 2000s through the pioneering works of Yeh *et al.*[1] and Cantor *et al.*[2] Initially introduced as multi-principal element alloys containing five or more elements in near-equiatomic proportions, HEAs marked a paradigm shift from conventional alloy design, which typically focused on one or two principal elements with minor additions.[3] Even though the foundational premise of HEAs—that high configurational entropy could stabilize simple solid solutions despite significant atomic size differences and diverse elemental interactions—has been shown to be a simplistic framework,[4,5] HEAs open unprecedented possibilities in metallurgical design.

The first decade of HEA research predominantly centred on mechanical properties, with extensive investigations into strength, ductility, hardness, wear resistance, and high-temperature stability.[6] These studies revealed exceptional combinations of properties, such as simultaneous strength and ductility, superior fracture toughness at cryogenic temperatures, and remarkable radiation resistance, positioning HEAs as promising candidates for structural applications in extreme environments.[7] It was not until the 2010s that significant attention shifted toward the functional properties of HEAs. Researchers began exploring magnetic,[8,9] catalytic,[10] hydrogen storage,[11] thermoelectric,[12] and radiation-resistant properties,[13] gradually expanding the application spectrum of these complex alloys. This functional-property exploration coincided with increasing capabilities to fabricate HEAs at the nanoscale, enabling entirely new application domains where surface area, quantum effects, and morphological control become critical design parameters.

The translation of HEA concepts to the nanoscale has presented both opportunities and challenges in materials science.[14] As revealed in recent comparative studies, HEA nanoparticle synthesis methods can be broadly categorized into top-down and bottom-up approaches, each with distinct advantages and limitations. Bottom-up synthesis techniques, including hot injection, carbothermal shock synthesis, and microwave heating, have demonstrated superior process control and promote atomic-level mixing. Recent studies by Dey *et al.*[15] and Yang *et al.*[16] have reported homogeneous elemental distribution through these approaches, while Qiao *et al.*[17] achieved uniform ~12 nm particles using microwave heating with roll-to-roll compatibility. These methods generally favour compositional uniformity and offer potential for scalable production.

In contrast, top-down approaches such as pulsed laser ablation in liquids (PLAL) typically yield particles with broader size distributions (2–120 nm), with narrower distributions obtained by Waag[18] and Löffler,[19] and may result in compositional heterogeneity or core–shell configurations. Nevertheless, as demonstrated by Tahir *et al.*,[20] these methods can be cost-efficient when process parameters are optimised. Among the emerging synthesis routes, electric discharge in dielectric liquids represents a promising yet underexplored approach. This method combines aspects of plasma-based techniques with liquid-phase processing, potentially offering rapid quenching rates, precise compositional control, and ambient processing conditions without requiring vacuum systems.[21,22]

Despite growing interest in HEA nanoparticles, their optical properties remain a largely unexplored field in materials science. The current literature on HEA optical properties is sparse and fragmented across different compositions, morphologies, and spectral ranges, creating a significant knowledge gap for applications in light conversion, sensing, and photonics. Recent studies demonstrate that HEAs exhibit wavelength-dependent optical behaviours modulated by composition and microstructure. In the visible and near-infrared regions, optical responses have been observed in HEA thin films with structural phase variations and nanotwin features,[23] while saturable absorption with modulation depths of 7.61% at 1 μm and 30.47% at 1.5 μm has enabled ultrashort fiber-laser pulses.[24] Deep-ultraviolet measurements on aluminium-rich alloys have revealed reflectance up to three times that of gold,[25] supported by dielectric-constant estimates from Drude/Lorentz models. In the terahertz domain, experiments on Nb–Mo–Ta–W thin films indicate high refractive indices that increase with film thickness, alongside rising extinction coefficients and conductivity.[26] For bulk high-entropy borides, low thermal emittance (0.12) and solar absorption (approximately 0.4) have been observed over the 0.3–16 μm range.[27]

In contrast to conventional plasmonic/metallic nanoparticles, fundamental optical characterization data such as ellipsometry measurements and explicit scattering and absorption cross-sections of HEA remain largely unreported in the literature. This absence of comprehensive optical property data presents a significant barrier to the development of HEA nanoparticles for photonic and plasmonic applications. This study aims to address the critical knowledge gaps regarding optical properties of HEA nanoparticles. Specifically, we investigate the electric discharge method in dielectric liquids as a versatile approach for producing compositionally uniform HEA nanoparticles. Furthermore, we present a systematic characterization of their optical properties, with particular focus on light-conversion applications through scattering and absorption mechanisms.

Methods

Nanoparticle synthesis and characterisation

The high-entropy alloy nanoparticles were synthesized using an electric discharge method in cryogenic dielectric liquids, as previously described by Hamdan *et al.*,[22] in which different dielectric liquids have been tested: pure water, heptane and liquid nitrogen. Liquid nitrogen avoids high-temperature oxidation during the process, like for water, or important carbon contamination, like for heptane. The experimental setup consisted of a high-DC-voltage power supply (Technix SR15-R-1200, 15 kV to 80 mA) connected to a solid-state switch (Behlke HTS-301-03-GSM), which delivered electrical pulses to one electrode, while the second electrode was grounded (Fig. 1a). This configuration produced a voltage rise time of 30 ns (Fig. 1b). Both electrodes were fabricated from a Cantor alloy ($Fe_{23.8}Co_{22.8}Cr_{22.3}Mn_{12.0}Ni_{19.1}$) and arranged in a pin-to-pin configuration while immersed in liquid nitrogen, which served as the dielectric medium. The characterisation of the Cantor alloy is available in Ledieu *et al.*[28]

The discharge dynamics were captured using a high-speed camera (FASTCAM SA5 model 1000K-M3) operating at 30 000 images per second. As illustrated in Fig. 1c, the sequence reveals the temporal evolution of the discharge process. Initially, intense plasma ignition occurs between the electrodes, generating

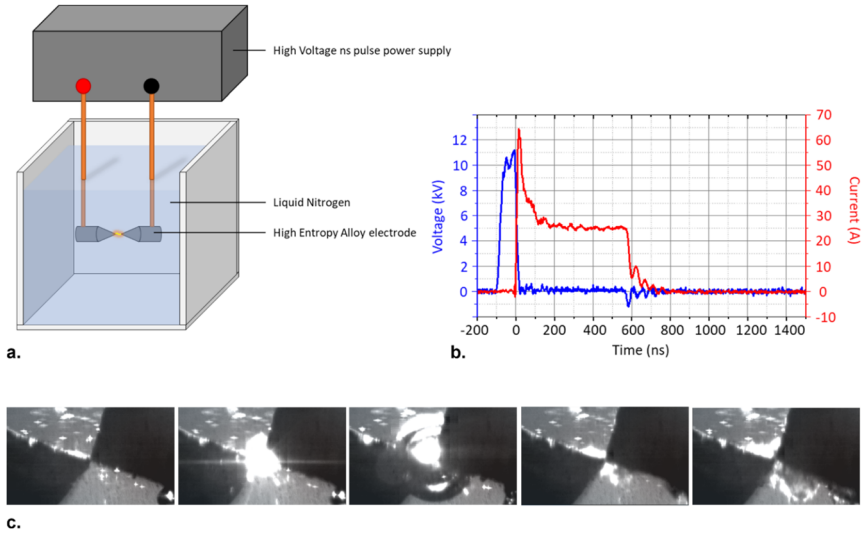

Fig. 1 Experimental setup and discharge dynamics for HEA nanoparticle synthesis *via* electric discharge in liquid nitrogen. (a) Schematic of the pin-to-pin electrode configuration with high-voltage pulse power supply and liquid nitrogen medium. (b) Voltage (blue) and current (red) profiles during a discharge event, showing a rapid rise time of 30 ns. (c) High-speed camera sequence (30 000 fps) capturing plasma ignition between the electrodes, followed by vapor-bubble formation, expansion, and collapse within tens of microseconds.

a bright emission zone. This is rapidly followed by the formation of a vapor bubble that expands outward from the discharge channel. The bubble continues to grow until reaching a maximum size, after which it undergoes collapse and subsequent oscillations. This entire cycle of bubble expansion and contraction occurs within a few tens of microseconds after the termination of the electrical discharge, as correlated with the voltage and current profiles shown in Fig. 1b. These rapid thermodynamic changes in the vicinity of the plasma channel create extreme synthesis conditions that facilitate the formation of HEA nanoparticles. Chen *et al.*[29] recently predicted thousands of possible HEAs stable at 0.9 T_m, yet many of them become metastable at room temperature. The ultrafast quenching rates inherent to plasma discharges limit atomic diffusion and prevent the system from reaching the equilibrium multiphase state dictated by thermodynamics. Instead, they open a kinetic pathway in which metastable solid solutions can nucleate and grow, consistent with the "metastability window" described in classical continuous-cooling diagrams and illustrated by Yao *et al.*[10] for HEA nanoparticles. This underscores the potential of non-equilibrium processes[30] such as using plasma, laser or ultrasound to access nano-HEAs that cannot be obtained under equilibrium conditions.

The nanoparticles generated during the discharge process were collected *via* sedimentation onto a silicon wafer positioned at the bottom of the Dewar vessel. After the complete evaporation of the liquid nitrogen, the particles were transferred to carbon grids for subsequent analysis by gently rubbing the silicon surface. The morphological, structural, and compositional characterization was

performed using high-resolution transmission electron microscopy (HRTEM) on a JEOL ARM 200F cold field-emission gun TEM/STEM operating at 200 kV with a point resolution of 0.12 nm. The microscope was equipped with a GIF quantum ER model 965 for enhanced imaging capabilities. Additionally, high-angle annular dark-field imaging in scanning TEM mode (HAADF/STEM) was combined with two-dimensional elemental mapping using energy-dispersive X-ray spectroscopy (EDX) to analyse the chemical composition and elemental distribution within the synthesized nanoparticle.

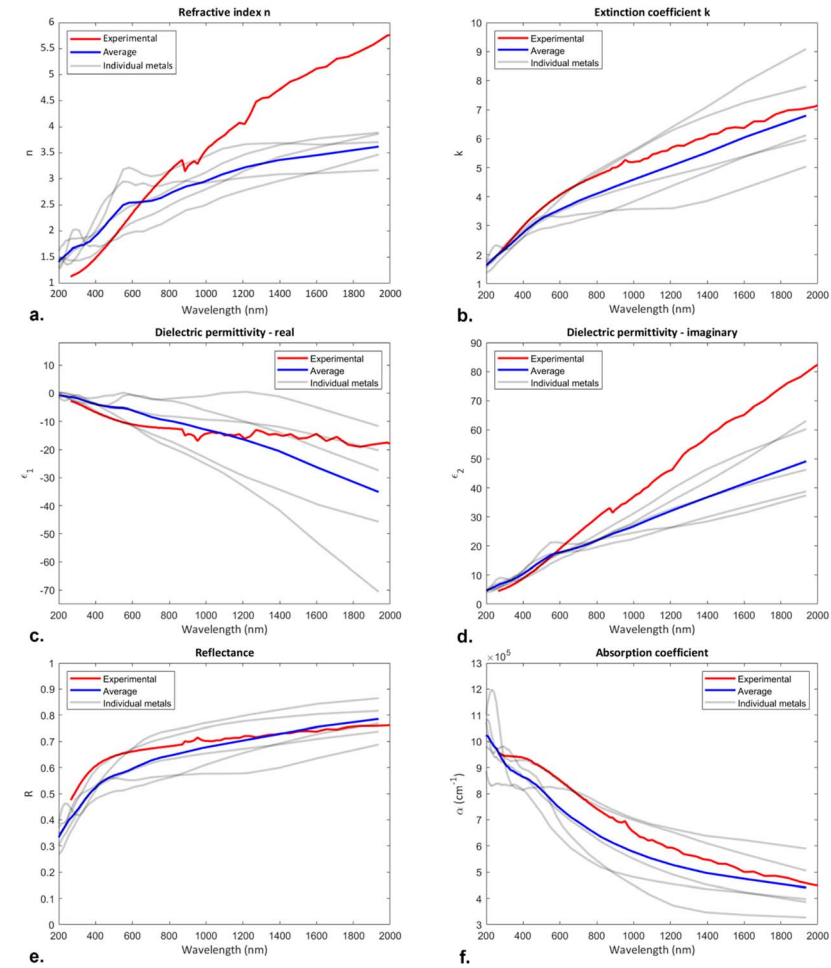

Fig. 2 Optical properties of bulk equiatomic CrMnFeCoNi Cantor alloy compared to constituent elements. (a) Refractive index (n), (b) extinction coefficient (k), (c) real part of the dielectric permittivity (ε_1), (d) imaginary part of the dielectric permittivity (ε_2), (e) reflectance (R), and (f) absorption coefficient (α) as functions of wavelength across 200–2000 nm. Red curves represent experimental measurements of the Cantor alloy, blue curves show the arithmetic average of constituent elements, and grey curves correspond to individual constituent metals. Note the significant deviation of fundamental optical constants (n, ε_2) from averaging, particularly in the infrared region, while functional properties (reflectance, absorption coefficient) closely follow the arithmetic mean.

Ellipsometry

Ellipsometric spectra for bulk HEA were acquired using a phase-modulated ellipsometer (UVISEL, HORIBA) at incidence angles of 50° and 70° across the 270–2100 nm spectral range. The measurement provides two ellipsometric parameters, ψ and Δ, at each wavelength. These parameters correspond directly to the ratio ρ between the Fresnel reflection coefficients r_p and r_s:

$$\rho = \frac{r_p}{r_s} = \tan(\psi)e^{j\Delta}$$

For the analysis, the HEA surface was considered sufficiently thick and opaque to be modelled as a semi-infinite medium. Under this assumption, the complex dielectric function (ε) of the material can be determined using the following equation:

$$\varepsilon = \sin^2(\theta)\left(1 + \left(\frac{1-\rho}{1+\rho}\right)^2 \tan^2(\theta)\right)$$

Here, θ represents the angle of incidence. From this equation, both real and imaginary components of the complex dielectric function are determined (Fig. 2c and d).

Optical dark-field

The optical resonances of individual HEA nanoparticles were characterized using white-light scattering measurements in the confocal dark-field configuration. Sample preparation involved depositing a solution droplet onto a fused-silica substrate and allowing the solvent to evaporate, resulting in isolated nanoparticles with a low surface density (approximately 0.1 particle per μm^2). The measurements utilized a custom-built dark-field setup[31] where s- or p-polarized illumination from a halogen lamp source (HL-2000-FHSA) was directed onto the sample at a 65° angle relative to the substrate normal. The scattered light was collected using a Mitutoyo M Plan APO NIR 50 objective with a numerical aperture of 0.45. Spectral analysis was performed using a Horiba LabRam HR confocal spectrometer equipped with a cooled Andor DU 420A-OE 325 CCD camera and a diffraction grating featuring 600 grooves per mm.

Results

Optical properties of high-entropy alloys

The optical properties of the equiatomic CrMnFeCoNi Cantor alloy were measured across the 200–2000 nm spectral range and compared with both its constituent elements and their arithmetic average. As shown in Fig. 2, the Cantor alloy exhibits typical optical behaviour of metals characterized by a relatively high refractive index, significant extinction coefficient, negative real part of the dielectric permittivity in the visible-NIR region, and strong absorption. In more detail, Fig. 2a reveals that the refractive index (n) of the Cantor alloy significantly deviates from the average of its constituent elements, particularly at longer wavelengths. In the infrared region (>1000 nm), the measured refractive index reaches values exceeding 5.5, substantially higher than both the individual metals

and their average (approximately 3.5). Similarly, the imaginary part of the dielectric function (ε_2) shown in Fig. 2d demonstrates considerable deviation from the average value, with the experimental curve displaying nearly twice the magnitude of the arithmetic mean in the near-infrared region. This deviation from the averaging is more limited in the case of the extinction coefficient (k) and the real part of the dielectric permittivity (ε_1), as illustrated in Fig. 2b and c, respectively.

Interestingly, despite these significant deviations in fundamental optical constants, the functional optical properties like the reflectance (Fig. 2e) and absorption coefficient (Fig. 2f) demonstrate remarkably close agreement between the measured values and the average of the constituent elements. This surprising result suggests that while the intrinsic optical constants (n, k, ε_1 and ε_2) of high-entropy alloys cannot be accurately predicted through the averaging, their macroscopic optical responses potentially could be.

Although the physics behind this observation requires some further study, a mathematical explanation could be proposed. We denote the alloy's complex refractive index with $\tilde{n} = n + ik$, and the arithmetic average of the constituents with $\tilde{n}_{avg} = n_{avg} + ik_{avg}$. Writing the alloy values as deviations from the average ($n = n_{avg} + \delta n$, $k = k_{avg} + \delta k$), the Fresnel reflectance at normal incidence is:

$$R(n,k) = \frac{(n-1)^2 + k^2}{(n+1)^2 + k^2}$$

A first-order Taylor expansion around (n_{avg}, k_{avg}) gives:

$$R \approx R_{avg} + \left.\frac{\partial R}{\partial n}\right|_{avg,} \delta n + \left.\frac{\partial R}{\partial k}\right|_{avg,} \delta k + O(\delta^2)$$

With $A = (n-1)^2 + k^2$ and $B = (n+1)^2 + k^2$, the partial derivatives are:

$$\frac{\partial R}{\partial n} = \frac{2(n-1)B - 2(n+1)A}{B^2}$$

$$\frac{\partial R}{\partial k} = \frac{8nk}{B^2}$$

Evaluated at the average point, the linear correction depends on δn, δk. If linear averaging of (n,k) is exact, $\delta n = \delta k = 0$ and the first-order term vanishes. More generally, because $R(n,k)$ is a smooth rational function, the error from using (n_{avg}, k_{avg}) is second-order in δ, which explains the close agreement seen for R and α compared to n and ε. For the absorption coefficient, $\alpha = 4\pi k/\lambda$, the first-order variation is simply $\delta\alpha = (4\pi/\lambda)\,\delta k$.

To test whether the Cantor behaviour is unique to that alloy or representative of a broader trend, we examined several binary alloys for which full optical constants are available in the Refractiveindex.info open database.[32] Four alloys are chemically disordered solid solutions—Au–Ag,[33] metastable Cu–Ag,[34] Fe–Ni (80% Ni),[35] and α-brass Cu–Zn[32] (70–90% Cu)—and two are ordered intermetallics, $PtAl_2$ and $AuAl_2$.[36] The evolution of the absorption coefficient with the

wavelength of all six binaries is plotted in Fig. 3. The corresponding n, k, ε_1, ε_2 and R appear in the SI. For Au–Ag (Fig. 3a) and Cu–Ag (Fig. 3b), the alloy curves lie entirely within the envelope defined by the two pure elements and shift smoothly toward the element that is enriched. The single Fe–Ni (Fig. 3c) composition fits the same envelope, suggesting the trend persists in this system. Cu–Zn (Fig. 3d) is less conclusive: its alloy spectrum sits closer to Cu than to Zn and shows no monotonic evolution, but the reports from which the optical constants are extracted lack phase characterisation, so partial ordering cannot be ruled out.

The intermetallics behave very differently; the plots of both $PtAl_2$ and $AuAl_2$ (Fig. 3e and f) are far outside their elemental envelopes, confirming that long-range order introduces new electronic bands and invalidates any linear mixing law. Taken together—one HEA and six binaries—the data support the use of

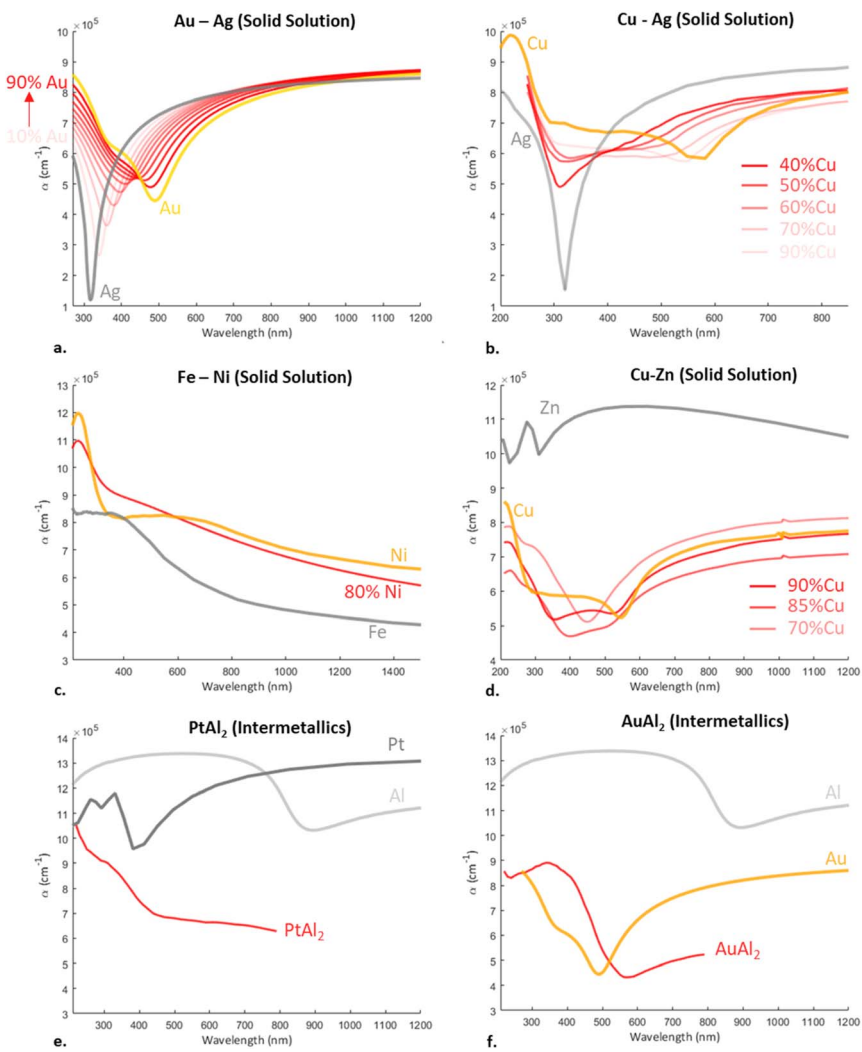

Fig. 3 Absorption coefficient of several selected alloys: (a) Au–Ag, (b) Cu–Ag, (c) Fe–Ni, (d) Cu–Zn, (e) $PtAl_2$ and (f) $AuAl_2$.

simple arithmetic averaging as a first-order proxy for the absorption coefficient and reflectance of disordered solid-solution alloys, while underscoring that it cannot be applied to ordered intermetallics.

Transitioning from bulk properties to nanoscale synthesis, we investigated nanoparticles generated by the electric discharge method in liquid nitrogen. The process produces CrMnFeCoNI high-entropy alloy nanoparticles with diameters ranging from 10 to 500 nm. Electron-diffraction analysis (Fig. 4b) confirmed the

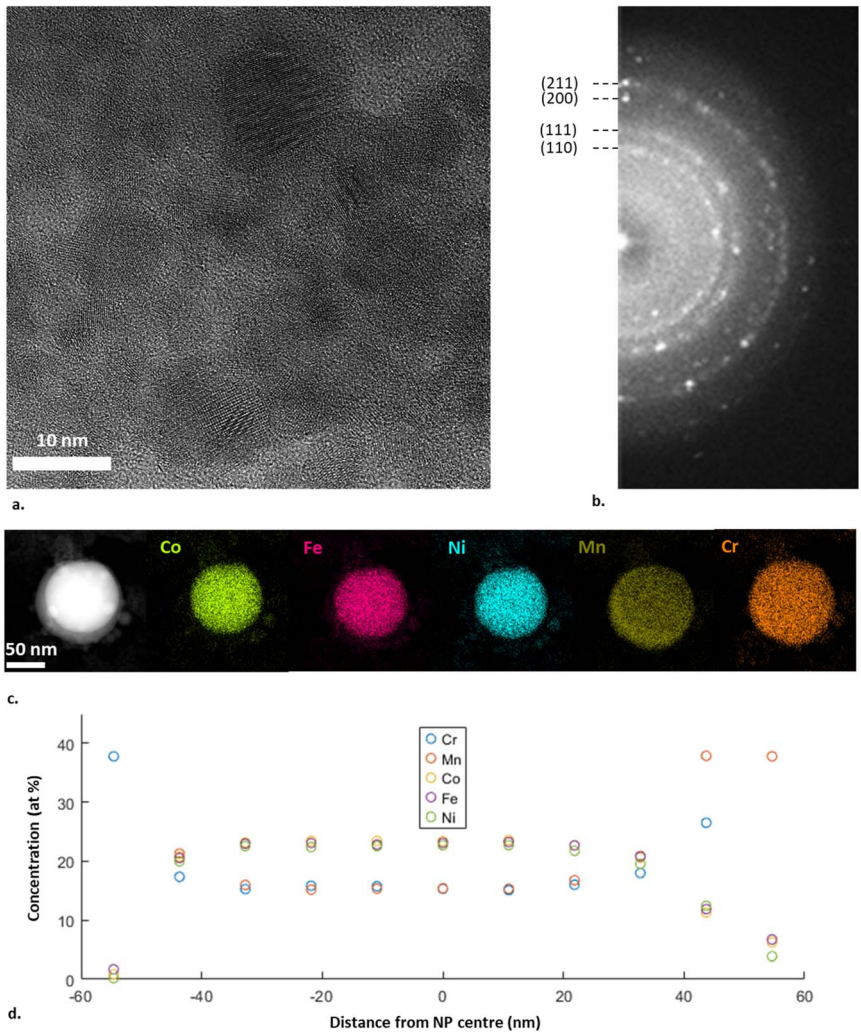

Fig. 4 Structural and compositional analysis of HEA nanoparticles synthesized *via* electric discharge. (a) HR-TEM micrograph showing crystal lattice of smaller nanoparticles (scale bar: 10 nm). (b) Selected-area electron diffraction pattern from multiple NPs with visible {110}, {111}, {200}, and {211} reflections, confirming a face-centered cubic structure with a lattice constant of ~360 pm. (c) HAADF-STEM micrograph with EDX elemental mapping showing uniform distribution of all five constituent elements (Co, Fe, Ni, Mn and Cr) throughout a representative nanoparticle (scale bar: 50 nm). (d) Elemental-line profiling over the nanoparticle.

crystalline nature of these nanoparticles, revealing a face-centred cubic structure with a lattice constant of approximately 360 pm, which closely matches that of the bulk Cantor alloy. Spatial distribution analysis of the chemical elements *via* energy-dispersive X-ray spectroscopy (Fig. 4c and d) demonstrates that the composition of the nanoparticles remains close to that of the electrode material. It is worth noting that a few-nm-thick oxide shell of Mn and Cr is observed on the nanoparticles (Fig. 4c and d), which is consistent with observations by other authors.[37,38] This can be attributed to their brief exposure to atmospheric conditions during transfer to the TEM grid, rather than oxidation during the synthesis process itself. Elemental-line profiling (Fig. 4d) shows that the surface enrichment of Mn and Cr is balanced by a few-percent depletion in the particle core, but the overall composition remains close to the target. Such thin oxide layers are common for metal nanoparticles and, given their small volume fraction, are not expected to significantly perturb the scattering signal. A quantitative assessment would require the wavelength-dependent optical constants of the mixed (Mn,Cr) oxide, which are not yet available; modelling the oxide contribution is therefore deferred to future work.

The optical properties of individual Cantor alloy nanoparticles were investigated using optical dark-field scattering spectroscopy. As shown in Fig. 5a, the dark-field image reveals that HEA nanoparticles of different radii scatter light at different wavelengths, resulting in a variety of colours visible across the field of

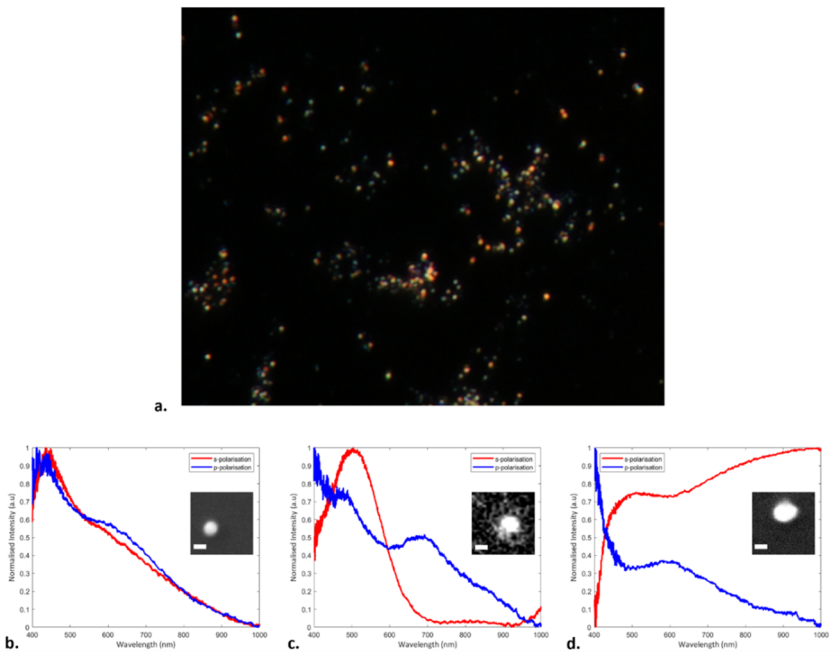

Fig. 5 Dark-field optical characterization of individual HEA nanoparticles. (a) Dark-field microscopy image showing multi-coloured scattering from HEA nanoparticles of various radii. Polarization-resolved scattering spectra of particles with radii of (b) 115 nm, (c) 140 nm, and (d) 180 nm, revealing size-dependent optical responses. Red and blue curves represent s-polarized and p-polarized illumination, respectively. Insets show dark-field images of the corresponding individual nanoparticles (scale bars: 100 nm).

view. This multicoloured appearance suggests size-dependent optical resonances, a combined feature of plasmonic and high-refractive-index nanostructures.

Polarization-resolved scattering spectra were collected from individual nanoparticles of different radii to quantify their optical response. Fig. 5b presents the scattering spectrum of a 115 nm radius nanoparticle, showing relatively similar responses for s-polarized (red) and p-polarized (blue) illumination, with a gradual decrease in scattering intensity toward longer wavelengths. In contrast, the medium-sized particle (140 nm radius) shown in Fig. 5c demonstrates strongly polarization-dependent scattering. Under s-polarized illumination, a pronounced peak appears around 500 nm, followed by a rapid decrease in intensity at longer wavelengths. Meanwhile, the p-polarized response shows a broader spectral distribution with a secondary resonance emerging around 750 nm, suggesting the excitation of higher-order optical modes. For the largest particle (180 nm radius) depicted in Fig. 5d, the polarization dependence becomes even more pronounced. The s-polarized spectrum shows a significant red-shift with increasing intensity toward the near-infrared region. Simultaneously, the p-polarized response exhibits a complex spectral shape with multiple resonances across the visible range, followed by a gradual decrease in intensity beyond 700 nm. Such differences generally arise from a combination of factors: the influence of the silica substrate on the nanoparticle resonances, variations in nanoparticle radius, and differences in the experimental geometry for optical excitation and for collecting the scattered light within a limited solid angle.

To understand the underlying mechanisms of light interaction with HEA nanoparticles, we performed a calculation of the optical cross-sections across different radii using the experimental optical indexes represented in Fig. 2. Fig. 6 presents a comprehensive analysis of the scattering and absorption behaviours as a function of the nanoparticle size. Fig. 6a–e show the evolution of the scattering (σ_{sca}), absorption (σ_{abs}), and extinction (σ_{ext}) cross-sections for HEA nanoparticles ranging from 50 nm to 1000 nm in radius. For the smallest particles ($R = 50$ nm, Fig. 6a), the spectra exhibit characteristic Rayleigh scattering behaviour with cross-sections scaling as λ^{-4}, and absorption dominating over scattering. As the particle size increases to 100 nm radius (Fig. 6b), we observe the emergence of spectral features associated with Mie scattering, including resonant peaks and a more complex wavelength dependence. At 200 nm radius (Fig. 6c), distinct Mie resonances become prominent in the visible and near-infrared regions, with scattering now significantly exceeding absorption. This trend continues with a further size increase to 500 nm (Fig. 6d), where multiple overlapping resonances create a broader spectral response. Finally, at the micrometre scale ($R = 1000$ nm, Fig. 6e), the nanoparticle enters the geometrical optics regime characterized by wavelength-independent cross-sections and predominantly forward scattering. Additionally, we illustrate in Fig. 6f the electric field distribution around a 100 nm radius nanoparticle at 570 nm wavelength, displayed in two orthogonal planes. The *XZ* plane clearly reveals an electric dipole mode with strong field enhancement at the nanoparticle–air interface.

Quantitative agreement between optical models and experiments is hampered by substrate interactions and by the collection efficiency of the dark-field set-up. Nevertheless, both simulation and measurement concur on a key trend: the dominant scattering mode appears for particles close to 100 nm in diameter and then red-shifts while broadening as the particle radius increases.

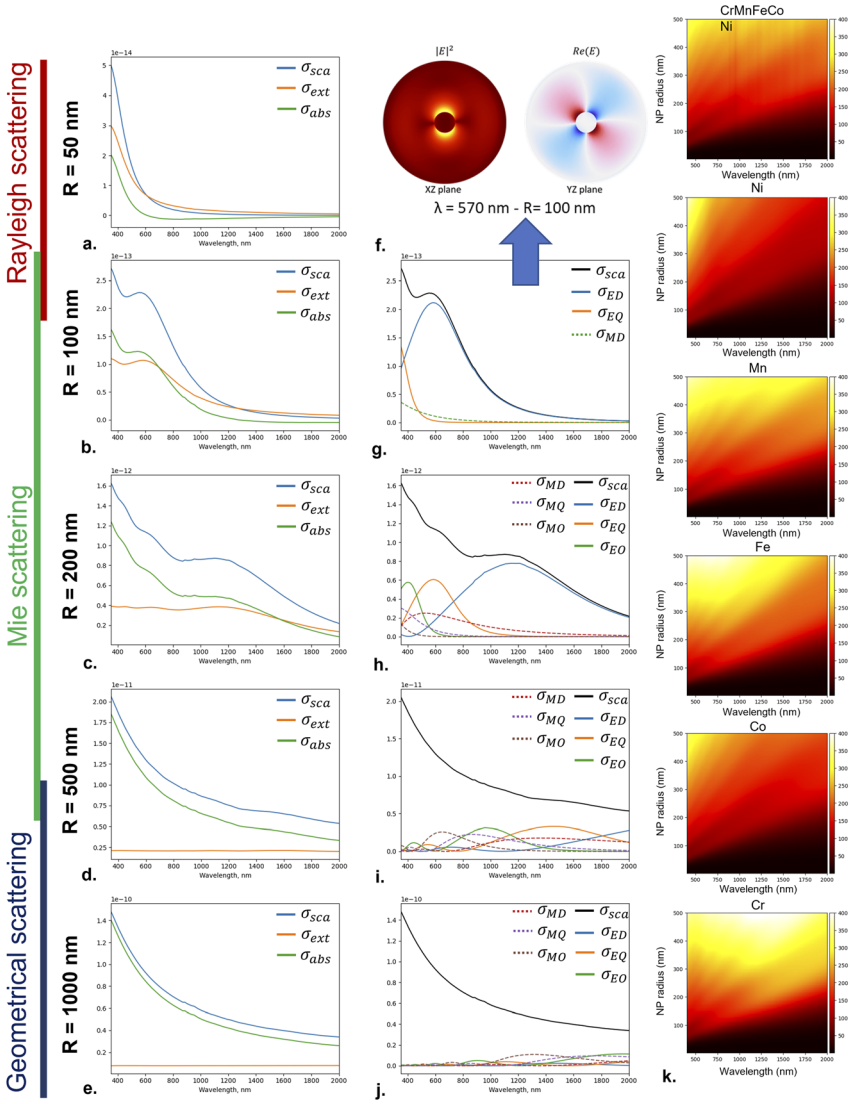

Fig. 6 Calculation of optical cross-sections and field distributions for HEA nanoparticles of different sizes. (a–e) Evolution of scattering (σ_{sca}, blue), absorption (σ_{abs}, green), and extinction (σ_{ext}, orange) cross-sections for nanoparticles with radii of 50, 100, 200, 500, and 1000 nm, showing transitions from Rayleigh to Mie and then to geometrical scattering regimes. (f) Electric field distribution around a 100 nm radius nanoparticle at 570 nm wavelength in the *XZ* and *YZ* planes, revealing dipole-like behaviour. (g–j) Multipole decomposition of scattering cross-sections for nanoparticles of increasing size, showing contributions from various electric and magnetic modes (E: electric mode, M: magnetic mode, D: diplole, Q: quadrupole, O: octupole) (k) Temperature elevation of nanoparticles as a function of their radius and the incident wavelength for an incident power of $I = 0.1\ \mu W\ \mu m^{-2}$.

The steady-state temperature rise, ΔT, of an isolated nanoparticle under continuous-wave illumination can be estimated from its absorption cross-section, σ_{abs}:

$$\Delta T = \frac{\sigma_{abs} \cdot I}{4\pi\kappa R}$$

with $\kappa = 0.0262$, the thermal conductivity of the surrounding medium (air, 1 bar, 300 K), and I, the irradiance, set to 0.1 μW μm^{-2}. Using σ_{abs} values derived from Mie theory, we find that the temperature elevation predicted for the high-entropy alloy (HEA) particles lies between those calculated for the individual constituent metals, consistent with their intermediate optical absorption (Fig. 6k).

Discussion and perspective

High-entropy alloys (HEAs) have greatly enlarged the compositional landscape available to materials scientists, but the thermodynamic and property-governing principles that operate in this multidimensional space are still only partially understood. Between 2015 and 2018, several systematic surveys demonstrated that configurational entropy is not by itself sufficient to stabilise single-phase solid solutions, contradicting the earliest HEA models.[4,5,39]

These findings coincided with the emergence of data-driven materials science (*e.g.*, machine learning) and encouraged the use of computationally inexpensive descriptors (a.k.a. features) to navigate vast compositional space. In this context a feature is a physically motivated, rapidly calculated surrogate (proxy descriptor) for a more complex quantity; it need not be exact, but it must capture the dominant trend at a fraction of the cost of full thermodynamic or electronic-structure calculations. For instance, the most classical features are the average and standard deviation of quantities like atomic radius, electronegativity, valence electron concentration (VEC) or melting point of the pure elements composing the HEA.

Following this approach and guided by the experimental study of the Cantor alloy, we adopt such a descriptor for optical screening. The results in Fig. 2 and 3 suggest that averaging the absorption coefficient and the reflectance of the pure elements could be a first-principle proxy for the exploration of the optical properties of HEA. The proxy of the absorption coefficient of HEA – α^{HEA} – is defined as follows:

$$\alpha^{HEA}(\lambda) = \sum_i x_i \cdot \alpha_i(\lambda)$$

with x_i the atomic concentration of the element i within the HEA. Similarly, the proxy of the reflectance, R^{HEA}, is:

$$R^{HEA}(\lambda) = \sum_i x_i \cdot R_i(\lambda)$$

To give a comprehensive overview of the possible optical properties of the HEAs, the 40-element palette selected by Chen *et al.*[29] has been used. This represents $\binom{40}{5} = 658\,008$ possible equimolar alloys. The stability of the possible crystallographic phases has been modelled using DFT for all these combinations by the same authors. This has led to a subset of 30 201 compositions for which a single-phase solid solution is stable at 0.9 T_m.

Within the 40-element palette, the optical indexes could be found for 30 of them in the Refractiveindex.info database,[32] which made it possible to calculate the absorption and reflectance proxy for 10 994 alloys predicted as HEAs (Fig. 7).

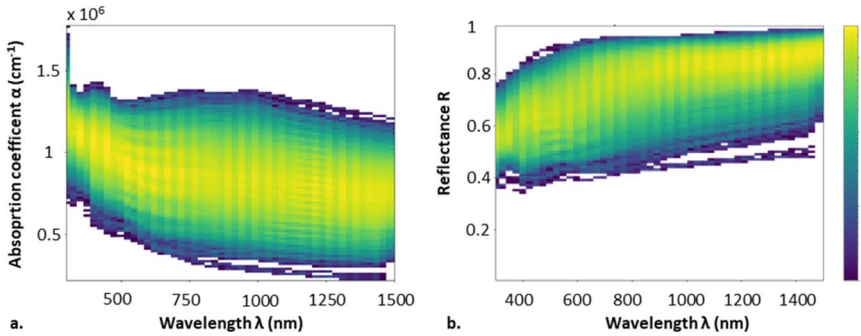

Fig. 7 Calculation of the (a) absorption and (b) reflectance proxy within the 300–1500 nm spectral range, for 10 994 HEAs.

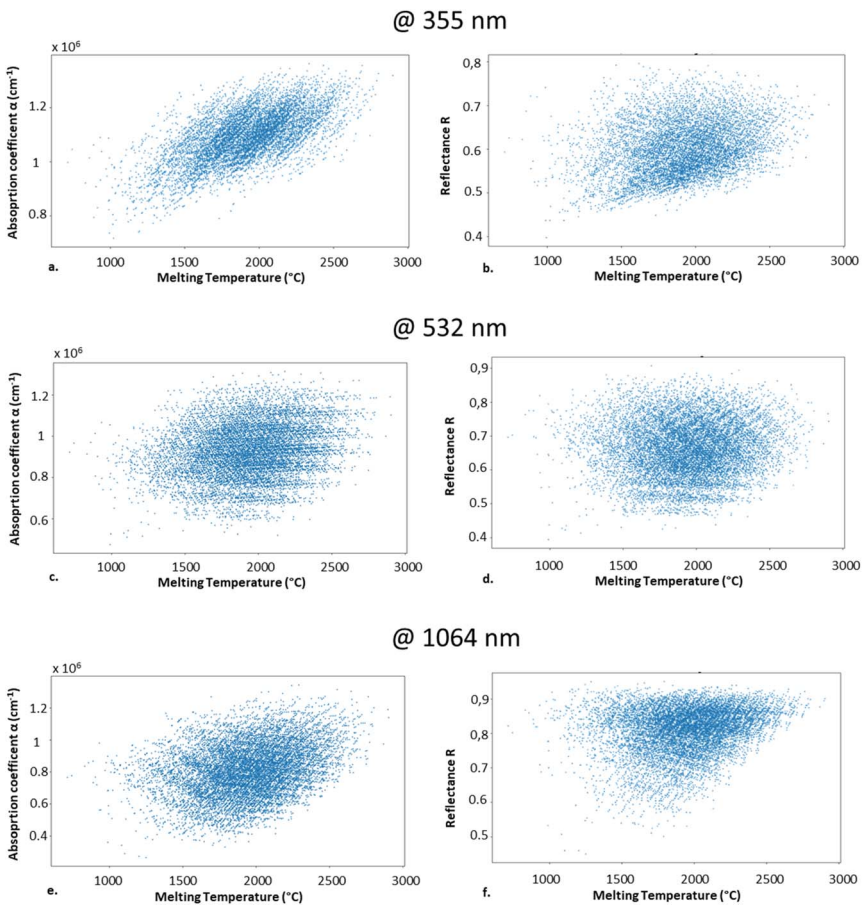

Fig. 8 Absorption coefficient and reflectance of 10 994 HEAs compared with the average melting point of their elements at 355 nm (a and b), 532 nm (c and d), and 1064 nm (e and f).

In sight of a possible application of HEAs for high-temperature optical applications (*e.g.*, thermoplasmonics, photocatalysis), the absorption coefficient and the reflectance have been plotted with the average melting point at 355 nm (Fig. 8a and b), 532 nm (Fig. 8c and d) and 1064 nm (Fig. 8e and f).

The absorption coefficients of the HEAs stand within 0.75 to 1.3 $\times$ 10^6 cm^{-1} at 355 nm, 0.5 to 1.3 $\times$ 10^6 cm^{-1} at 532 nm, and 0.3 to 1.3 $\times$ 10^6 cm^{-1} at 1064 nm. The reflectance of the HEAs stands within 0.4 to 0.8 at 355 nm, 0.4 to 0.9 at 532 nm, and 0.45 to 0.95 at 1064 nm.

In Fig. 9, we showcase how these results could be used to identify regions of interest (ROI) to select the most promising subset of HEAs with an approach

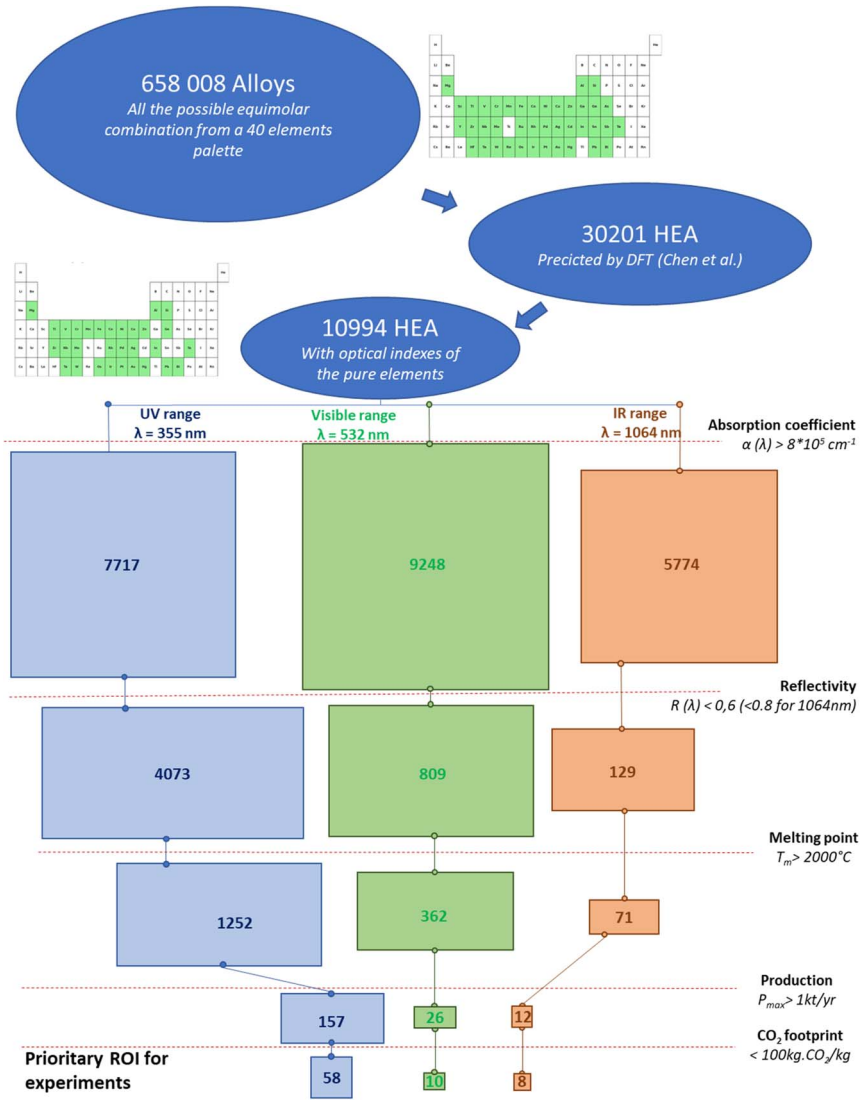

Fig. 9 Overview of a sustainable materials-by-design approach applied to sustainable HEAs for optical applications.

based on sustainable materials-by-design. This consists of refining of possible candidates according to successive screening steps. The screening criteria are of three kinds: thermodynamics, physical properties and sustainability. The selection of the 30 201 HEAs from all the possible quinary alloys has been described in a previous section. Regarding the physical properties, three criteria have been successfully applied:

• Absorption coefficient ($\alpha > 8 \times 10^5$ cm^{-1}): 7717 HEAs satisfy this criterion at 355 nm, 9248 at 532 nm and 5774 at 1064 nm.

• The reflectance filter has been set at 0.6, which is a moderate value that opens possibility for light-to-heat conversion. 4073 HEAs satisfy this second criterion at 355 nm and 809 at 532 nm. This threshold had to be increased up to 0.8 for 1064 nm so that 129 HEAs could be kept.

• Melting point ($T_m > 2000$ °C): this corresponds to the empirical definition of refractory alloys. In terms of application, this criterion largely overcomes the melting points of the most popular plasmonic materials ($T_m = 1064$ °C for Au, $T_m = 961$ °C for Ag, and $T_m = 660$ °C for Al) and of the typical photocatalyst TiO_2 ($T_m = 1843$ °C). This reduces the number of candidates to 1252, 362 and 71 respectively at 355, 532 and 1064 nm.

Following a recent overview of the sustainability of HEAs,[40] and from the perspective of an accelerated development of the alloys and the associated technology, we associated two sustainability criteria:

• Maximal production (>1 kton per year): this measures the maximum production of each HEA based on the scarcest element of the alloy. Maximum annual production potential for each HEA is calculated using the formula:

$$P_{\max}^{\mathrm{HEA}} = \min\left\{\frac{P_i}{x_i^{\mathrm{HEA}}}\right\}$$

where P_i is the global annual production of element i found in the US Geological Survey,[41] and x_i^{HEA} is the molar concentration of element i in the alloy. The threshold of 1000 tons does not necessarily mean that the targeted application will consume this amount. Indeed, conflicts of use are also to be taken into account. A 1000-ton threshold allows the development of an application generating a demand of 50–100 tons per year with a reasonable risk of usage conflict. This drastically reduces the set to 157, 26 and 12 HEAs, respectively, at 355, 532 and 1064 nm.

• CO_2 footprint (<100 kg CO_2 per kg): The environmental impact of the metal extraction cannot be neglected in the life-cycle assessment of the products. Mass carbon footprints F^{CO_2} per unit of mass of each metal m have been found in the commercial GrantaEduPack© Software, which gathers different sources. An alternative open-access database has been published by Nuss *et al.*[42] Carbon footprints have been converted into molar footprints f^{CO_2}. The footprints of an HEA j composed of n metals m in a concentration x have been calculated as follows:

$$f_{\mathrm{HEA}}^{\mathrm{CO_2}} = \sum_{m=1}^{n} x_m f_m^{\mathrm{CO_2}}$$

• A threshold of 100 kg CO_2 per kg may sound excessive as compared to that of the rock-forming elements like iron (approx. 2 kg CO_2 per kg) or aluminium (8–12

kg CO_2 per kg). This remains, however, two orders of magnitude below the values for gold and platinum (30–60 tons CO_2 per kg). This final criterion reduces the ROI to 58, 10 and 8 HEAs, respectively, at 355, 532 and 1064 nm. The list of HEAs satisfying all the criteria is given in the SI.

This example shows how a succession of simple calculations helps to rapidly identify a few tens of HEAs that could be of interest for a given set of properties. Indeed, the threshold could be modified for a targeted application, which would change the size and content of the ROI.

Such an approach would be powerful to develop experimentally for two purposes:

• Applicative: this approach ensures a broad and exclusive screening of the field of possibilities. Moreover, including sustainability, and particularly the resource availability, avoids costly research being inapplicable for real-life products due to lack of resources. This filtering is not made at the expense of the physical interest of the alloys, since these criteria are applied first. Sustainability is potentially accelerating larger-scale deployment without being a limitation for fundamental investigations.

• Fundamental: as mentioned above, the definitions of the descriptors (proxies) of the absorption coefficient and reflectance are based on observations on the Cantor alloy and not on a solid theoretical background. However, measurements of the optical properties of HEAs being too scarce, there is not yet an alternative at low computational cost. Once a reasonable subset of HEAs have been characterized, this subset could be used to validate or update this approach with more accurate descriptors, and also inspire more theoretical works on the optical properties of solid solutions.

Conclusions

Bulk ellipsometry provides the first complete set of optical constants for the equiatomic CrMnFeCoNi (Cantor) alloy. Although n and k differ strongly from the arithmetic averages of the constituent elements, the functional quantities of practical interest—normal-incidence reflectance R and absorption coefficient α—remain within $\approx 20\%$ of the linear-mixing estimate from 300 to 1500 nm.

Nanoparticles generated by liquid-nitrogen electric discharge inherit these bulk constants, enabling a first calculation of optically induced heating. We find that the HEA photothermal response is bounded by those of its pure constituents.

Finally, the validated averaging rule has been applied to 10 994 DFT-stable HEAs. When combined with melting-point, production-volume and CO_2-footprint filters, the search space contracts to fewer than 60 promising compositions, illustrating how accurate bulk optics, photothermal estimates, and sustainability criteria can be integrated into a coherent "sustainable materials-by-design" roadmap for future HEA photonic applications.

Author contributions

Conceptualization: AN, VM; data curation: AIS, MV, SB, JZ, YB, JG, UC, TB, JP; investigation: AN, VM, MV, SB, YB, JP, MF; methodology: AN, VM, YB, UC; writing – original draft: AN, VM; writing – review & editing: all authors; funding acquisition: JFP, TB, AN, VM.

Conflicts of interest

There are no conflicts to declare.

Data availability

Data for this article, including: high speed video recording of the dielectric discharge and bubble growth dynamics (folder Discharge); optical properties of bulk equiatomic CrMnFeCoNi Cantor and individual metals; refractive index (n), extinction coefficient (k), real part of dielectric permittivity (ε_1), imaginary part of dielectric permittivity (ε_2), reflectance (R), and absorption coefficient (α) as functions of wavelength across 200–2000 nm (folder Optics bulk); Transmission Electron Micrographs of nanoparticles (folder Nanoparticles); - scattering spectra of nanoparticles (folder Scattering); dataset containing the (folder Materials by Design): alloy composition, average absorption coefficient (in cm^{-1}), average reflectance; average melting point (in °C), CO_2 footprint in (kg CO_2 per kg), maximum production of the alloy in tons per year are available at Jožef Stefan Institute – F6 department repository at: **https://f6cloud.ijs.si/index.php/s/FRSiZCFFfkRi4yE**.

Supplementary information (SI) is available. See DOI: **https://doi.org/10.1039/d5fd00086f**.

Acknowledgements

AN, JFP and VM are thankful to Institut Carnot for Energy in Lorraine 'ICEEL' for financial support through TANNIC project. JZ and UC acknowledge support by Slovenian Research Agency (ARRS) program P1-0417 and project J2-4440 and by the European Innovation Council Pathfinder project under ThermoDust grant agreement No. 101046835. AN, JZ and UC are thankful to the European Union for financial support through the Erasmus Program 'Cooperation Partnership' (Project Title: HERawS – Highlights on European Raw materials Sustainability – Project No. 2022-1-FR01-KA220-HED-000087621).

Notes and references

1 J.-W. Yeh, *et al.*, Nanostructured High-Entropy Alloys with Multiple Principal Elements: Novel Alloy Design Concepts and Outcomes, *Adv. Eng. Mater.*, 2004, **6**, 299–303.
2 B. Cantor, I. T. H. Chang, P. Knight and A. J. B. Vincent, Microstructural development in equiatomic multicomponent alloys, *Mater. Sci. Eng., A*, 2004, **375–377**, 213–218.
3 D. B. Miracle, High entropy alloys as a bold step forward in alloy development, *Nat. Commun.*, 2019, **10**, 1805.
4 E. Menou, *et al.*, Computational design of light and strong high entropy alloys (HEA): Obtainment of an extremely high specific solid solution hardening, *Scr. Mater.*, 2018, **156**, 120–123.
5 O. N. Senkov, J. D. Miller, D. B. Miracle and C. Woodward, Accelerated exploration of multi-principal element alloys with solid solution phases, *Nat. Commun.*, 2015, **6**, 6529.

6 E. P. George, W. A. Curtin and C. C. Tasan, High entropy alloys: A focused review of mechanical properties and deformation mechanisms, *Acta Mater.*, 2020, **188**, 435–474.
7 Y. H. Jo, *et al.*, Cryogenic strength improvement by utilizing room-temperature deformation twinning in a partially recrystallized VCrMnFeCoNi high-entropy alloy, *Nat. Commun.*, 2017, **8**, 15719.
8 O. Schneeweiss, *et al.*, Magnetic properties of the CrMnFeCoNi high-entropy alloy, *Phys. Rev. B: Condens. Matter Mater. Phys.*, 2017, **96**, 014437.
9 J.-W. Chen, *et al.*, Role of the structure order in the transport and magnetic properties of high-entropy alloy films, *NPG Asia Mater.*, 2024, **15**, 1–8.
10 Y. Yao, *et al.*, Carbothermal shock synthesis of high-entropy-alloy nanoparticles, *Science*, 2018, **359**, 1489–1494.
11 F. Marques, M. Balcerzak, F. Winkelmann, G. Zepon and M. Felderhoff, Review and outlook on high-entropy alloys for hydrogen storage, *Energy Environ. Sci.*, 2021, **14**, 5191–5227.
12 X. Wang, *et al.*, Enhanced Thermoelectric Performance in High Entropy Alloys Sn0.25Pb0.25Mn0.25Ge0.25Te, *ACS Appl. Mater. Interfaces*, 2021, **13**, 18638–18647.
13 O. El-Atwani, *et al.*, Outstanding radiation resistance of tungsten-based high-entropy alloys, *Sci. Adv.*, 2019, **5**, eaav2002.
14 M. Y. Rekha, N. Mallik and C. Srivastava, First Report on High Entropy Alloy Nanoparticle Decorated Graphene, *Sci. Rep.*, 2018, **8**, 8737.
15 G. R. Dey, C. R. McCormick, S. S. Soliman, A. J. Darling and R. E. Schaak, Chemical Insights into the Formation of Colloidal High Entropy Alloy Nanoparticles, *ACS Nano*, 2023, **17**, 5943–5955.
16 Y. Yang, *et al.*, Aerosol Synthesis of High Entropy Alloy Nanoparticles, *Langmuir*, 2020, **36**, 1985–1992.
17 H. Qiao, *et al.*, Scalable Synthesis of High Entropy Alloy Nanoparticles by Microwave Heating, *ACS Nano*, 2021, **15**, 14928–14937.
18 F. Waag, *et al.*, Kinetically-controlled laser-synthesis of colloidal high-entropy alloy nanoparticles, *RSC Adv.*, 2019, **9**, 18547–18558.
19 T. Löffler, *et al.*, Comparing the Activity of Complex Solid Solution Electrocatalysts Using Inflection Points of Voltammetric Activity Curves as Activity Descriptors, *ACS Catal.*, 2021, **11**, 1014–1023.
20 S. Tahir, *et al.*, Synthesis of High Entropy Alloy Nanoparticles by Pulsed Laser Ablation in Liquids: Influence of Target Preparation on Stoichiometry and Productivity, *ChemNanoMat*, 2024, **10**, e202400064.
21 A. Hamdan, *et al.*, Interaction of micro-discharges in heptane with metallic multi-layers, *Appl. Surf. Sci.*, 2013, **274**, 378–391.
22 A. Hamdan, C. Noel, F. Kosior, G. Henrion and T. Belmonte, Impacts created on various materials by micro-discharges in heptane: Influence of the dissipated charge, *J. Appl. Phys.*, 2013, **113**, 043301.
23 S.-E. Benrazzouq, *et al.*, Tailoring the nonlinear optical response of high-entropy alloy thin films through compositional and structural modification, in *Advances in Optical Thin Films VIII*, SPIE, 2024, vol. 13020, pp. 76–80.
24 X. Liu, *et al.*, Enhanced Interband Transition in FeCoNiAlTi High-Entropy Alloy for Ultrafast Nonlinear Optical Applications, *Adv. Opt. Mater.*, 2024, **12**, 2302043.

25 C.-H. Yeh, *et al.*, Design of high-entropy films as ultra-violet light reflector, *Appl. Mater. Today*, 2024, **36**, 102013.
26 C.-Y. Lu, *et al.*, Terahertz characterization of nano-scale high-entropy alloy films and their high-contrast grating applications, *AIP Adv.*, 2024, **14**, 035036.
27 S. Barbarossa, *et al.*, Optical properties of bulk high-entropy diborides for solar energy applications, *J. Alloys Compd.*, 2023, **935**, 167965.
28 J. Ledieu, *et al.*, The (110) and (320) surfaces of a Cantor alloy, *Acta Mater.*, 2021, **209**, 116790.
29 W. Chen, *et al.*, A map of single-phase high-entropy alloys, *Nat. Commun.*, 2023, **14**, 2856.
30 I. Levchenko, *et al.*, Lightning under water: Diverse reactive environments and evidence of synergistic effects for material treatment and activation, *Appl. Phys. Rev.*, 2018, **5**, 021103.
31 P. A. Dmitriev, *et al.*, Laser fabrication of crystalline silicon nanoresonators from an amorphous film for low-loss all-dielectric nanophotonics, *Nanoscale*, 2016, **8**, 5043–5048.
32 M. N. Polyanskiy, Refractiveindex.info database of optical constants, *Sci. Data*, 2024, **11**, 94.
33 D. Rioux, *et al.*, An Analytic Model for the Dielectric Function of Au, Ag, and their Alloys, *Adv. Opt. Mater.*, 2014, **2**, 176–182.
34 J. Song, H. Li, J. Li, S. Wang and S. Zhou, Fabrication and optical properties of metastable Cu–Ag alloys, *Appl. Opt.*, 2002, **41**, 5413–5416.
35 K. K. Tikuišis, *et al.*, Optical And Magneto-Optical Properties Of Permalloy Thin Films In 0.7–6.4ev Photon Energy Range, *Mater. Des.*, 2017, **114**, 31–39.
36 L.-Y. Chen and D. W. Lynch, The Optical Properties of AuAl2 and PtAl2, *Phys. Status Solidi B*, 1988, **148**, 387–394.
37 C. Luan, *et al.*, Revealing Dynamic Surface and Subsurface Reconstruction of High-Entropy Alloy Electrocatalysts during the Oxygen Evolution Reaction at the Atomic Scale, *ACS Catal.*, 2024, **14**, 12704–12716.
38 V. Strotkötter, *et al.*, Self-formation of compositionally complex surface oxides on high entropy alloys observed by accelerated atom probe tomography: a route to sustainable catalysts, *Mater. Horiz.*, 2024, **11**, 4932–4941.
39 S. Gorsse and F. Tancret, Current and emerging practices of CALPHAD toward the development of high entropy alloys and complex concentrated alloys, *J. Mater. Res.*, 2018, **33**, 2899–2923.
40 A. Nomine, *et al.*, The most sustainable high entropy alloys for the future, *Research Square*, 2023, DOI: **10.21203/rs.3.rs-3553470/v1**
41 U. S. G. Survey, *Mineral Commodity Summaries 2024*, Mineral Commodity Summaries, 2024, preprint, DOI: **10.3133/mcs2024**, **https://pubs.usgs.gov/publication/mcs2024**.
42 P. Nuss and M. J. Eckelman, Life Cycle Assessment of Metals: A Scientific Synthesis, *PLoS One*, 2014, **9**, e101298.